Available online at www.sciencedirect.com
ScienceDirect
Journal of Structural Biology xxx (2006) xxx–xxx
Journal of Structural Biology
www.elsevier.com/locate/yjsbi

Electron energy filtering significantly improves amplitude contrast of frozen-hydrated protein at 300 kV

Koji Yonekura [a,*], Michael B. Braunfeld [b], Saori Maki-Yonekura [a,c], David A. Agard [b,d]

[a] The W.M. Keck Advanced Microscopy Laboratory, Department of Biochemistry and Biophysics, University of California, San Francisco, 1700, 4th Street, San Francisco, CA 94158-2532, USA
[b] Howard Hughes Medical Institute, University of California, San Francisco, 600 16th Street, San Francisco, CA 94158, USA
[c] Dynamic Nano Machine Project, ICORP, JST, 1-3 Yamadaoka, Suita, Osaka 565-0871, Japan
[d] The W.M. Keck Advanced Microscopy Laboratory, Department of Biochemistry and Biophysics, University of California, San Francisco, CA 94158-2240, USA

Received 18 April 2006; received in revised form 12 July 2006; accepted 18 July 2006

Abstract

The amplitude contrast of frozen-hydrated biological samples was measured using the bacterial flagellar filament embedded in vitreous ice at an accelerating voltage of 300 kV. From the mean radial amplitude spectra of overfocused images, amplitude contrast was estimated to be $6.9 \pm 1.9\%$ and $2.7 \pm 1.0\%$ of the whole contrast at the low spatial frequency range with and without energy filtering, respectively, and that of the carbon film to be $9.5 \pm 2.0\%$ and $5.8 \pm 1.8\%$. Energy filtering effectively doubled the signal-to-noise ratio in the images of frozen-hydrated filaments, and substantially improved intensity data statistics of layer lines up to at least ~25 Å resolution in their Fourier transforms. It also markedly improved inter-particle fitting phase residuals of averaged data at resolutions up to ~15 Å. Using the energy filtered data recorded on a new high-performance, lens-coupled CCD camera the three-dimensional map of the flagellar filament was calculated at 8 Å by applying the amplitude contrast of 6.9%. The map and its mean radial density distribution validated the obtained value of the amplitude contrast.

Keywords: Energy filtering; Cryo-electron microscopy; Amplitude contrast; Flagellar filament

1. Introduction

Cryo-electron microscopy is now being widely used to analyze biological macromolecular structures. In this method, specimens are embedded in a thin layer of vitreous ice and imaged at cryogenic temperatures with an electron microscope. It can allow direct observation of biological samples in a native state or a state close to it, although the image contrast is very poor. Here the contrast originates mainly from interference of unscattered electrons and those scattered by light atoms in the specimen. This is known as phase contrast. There is another source of the contrast, amplitude contrast, which arises from absorption of electrons in the specimen and loss of electrons scattered outside the objective aperture (''virtual absorption''). Although the amount of the amplitude contrast is much smaller than that of the phase contrast, it contributes to the overall density distribution, and becomes an important factor for reconstructing structures accurately. There have been a number of reports on the amplitude contrast of frozen-hydrated biological molecules (Toyoshima and Unwin, 1988; Smith and Langmore, 1992; Toyoshima et al., 1993; Zhu et al., 1997; Thuman-Commike et al., 1999; Angert et al., 2000; Sander et al., 2003; Mallick et al., 2005) and it was estimated to about a few to ten percents of the whole contrast. About half of those studies used computational model fitting. The amplitude contrast is dominant in the very low spatial frequency range, but there is high background arising from direct electron beam and inelastic scattering. As a

* Corresponding author. Fax: 1 415 514 2550.
E-mail address: yone@msg.ucsf.edu (K. Yonekura).

1047-8477/$ - see front matter © 2006 Elsevier Inc. All rights reserved.
doi:10.1016/j.jsb.2006.07.016

consequence, it is very difficult to estimate the amplitude contrast accurately from such data by model fitting. As an alternative, Toyoshima et al. (1993) used overfocused images, which have a zero-crossover point in their contrast transfer function at low spatial frequencies, and measured the amplitude contrast at accelerating voltages of 120 and 200 kV. They showed that the amplitude contrast decreases at higher accelerating voltages (Toyoshima et al., 1993).

Energy filtering can improve the image contrast of biological molecules embedded in ice (Fig. 1; Schröder et al., 1990; Langmore and Smith, 1992; Zhu et al., 1997) by removing inelastically scattered electrons. Not only will this reduce background noise but also it should enhance contrast due to the virtual absorption of electrons. There have been a few reports on measuring the amplitude contrast of filtered images by computational model fitting (Zhu et al., 1997; Angert et al., 2000) or from the mean radial density distribution (MRDD) of tobacco mosaic virus (Langmore and Smith, 1992). These studies reported an increase of amplitude contrast in the filtered image at accelerating voltages of 80 and 120 kV.

Here, we report direct measurements of amplitude contrast of frozen-hydrated protein with and without energy filtering at an accelerating voltage of 300 kV, which is becoming the standard for high-resolution structural analysis of biological molecules. The bacterial flagellar filament (Yonekura et al., 2003a) was used as a test specimen. We measured the amplitude contrast from the mean radial amplitude spectra of filament images taken at overfocus. Because this method can be applied to various types of samples, that of the carbon film was also measured. We also quantitatively demonstrated the improvement in contrast and signal-to-noise ratios (S/N) of the filtered images, and intensity data statistics (I/σ) and phase residuals of the layer lines in their Fourier transforms. Using a value thus obtained, the three-dimensional structure of the flagellar filament was calculated at 8 Å resolution, validating our measure of the amplitude contrast.

2. Methods

2.1. Theoretical background

After passing through the specimen, the electron waveform $\psi(\boldsymbol{r})$ at a position $\boldsymbol{r}$ can be described as

$$\psi(r) = \exp\{i\eta(\boldsymbol{r}) - \varepsilon(\boldsymbol{r})\}, \quad (1)$$

where $\eta(\boldsymbol{r})$ and $\varepsilon(\boldsymbol{r})$ represent a phase shift and an attenuation of the incident wave, respectively. In zero energy loss (zero-loss) imaging by energy filtering, the attenuation term, $\varepsilon(\boldsymbol{r})$ may be divided into two as

$$\varepsilon(\boldsymbol{r}) = \varepsilon_0(\boldsymbol{r}) + \varepsilon_{ef}(\boldsymbol{r}), \quad (2)$$

where $\varepsilon_0(\boldsymbol{r})$ represents the "usual" amplitude contrast in unfiltered imaging, which arises from electrons inelastically scattered or those scattered outside the objective aperture,

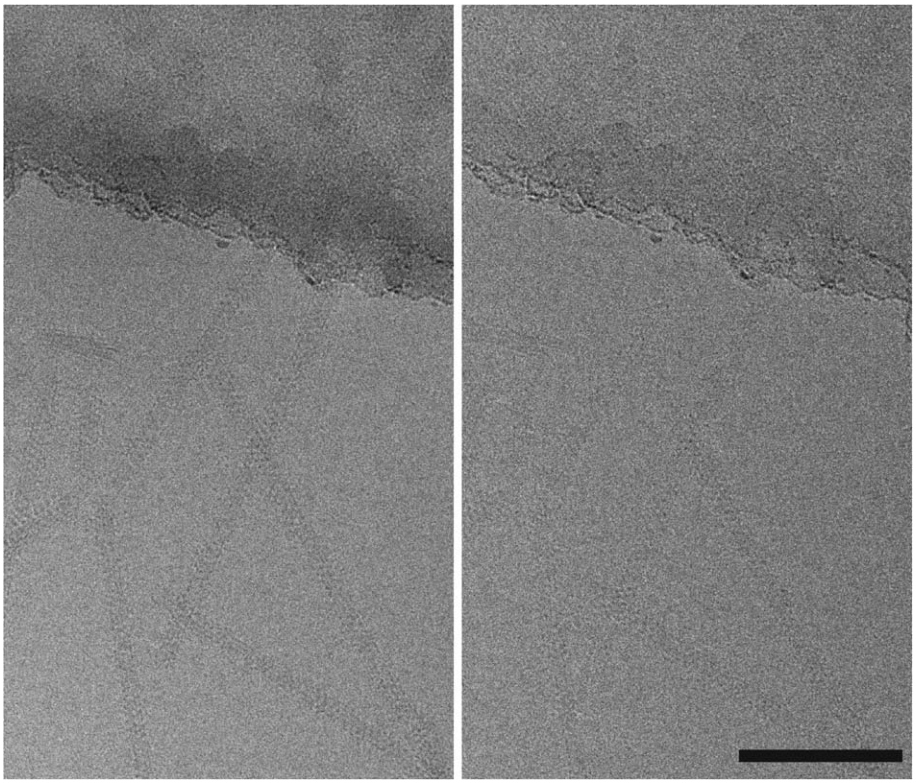

Fig. 1. Side by side comparison of electron micrographs of the bacterial flagellar filament recorded on a SSCCD camera at an accelerating voltage of 300 kV with energy filtering in the 1st exposure (left) and without it in the 2nd exposure (right). Defocus of ~17000 Å underfocus was used. Note that the contrast of the filaments and the edge of the carbon film is much higher in the filtered image (left). Bar represents 1000 Å.

Please cite this article as: Koji Yonekura et al., Electron energy filtering significantly improves amplitude ..., Journal of Structural Biology (2006), doi:10.1016/j.jsb.2006.07.016

and $\varepsilon_{ef}(\boldsymbol{r})$ further attenuation by energy filtering. In EM image formation, the weak-phase-weak-amplitude approximation is a good representation for bright-field imaging of thin specimens:

$$\psi(\boldsymbol{r}) = 1 + \mathrm{i}\eta(\boldsymbol{r}) - \varepsilon(\boldsymbol{r}). \tag{3}$$

Through the objective lens, the phase shifts introduced by spherical aberration and defocus into the wave function $\Psi(\boldsymbol{k})$ at a spatial frequency $\boldsymbol{k}$ in the diffraction plane can be written as,

$$\Psi(\boldsymbol{k}) = \{\delta(\boldsymbol{k}) + \mathrm{i}A(\boldsymbol{k}) - B_0(\boldsymbol{k}) - B_{ef}(\boldsymbol{k})\} \times \exp\{-\mathrm{i}\gamma(k)\}, \tag{4}$$

where $A(\boldsymbol{k})$, $B_0(\boldsymbol{k})$ and $B_{ef}(\boldsymbol{k})$ correspond to the Fourier transforms of $\eta(\boldsymbol{r})$, $\varepsilon_0(\boldsymbol{r})$ and $\varepsilon_{ef}(\boldsymbol{r})$, respectively. $\gamma(\boldsymbol{k})$ can be expressed as,

$$\gamma(k) = 2\pi(\tfrac{1}{4}Cs \cdot \lambda^3 \cdot k^4 - \tfrac{1}{2}\Delta f \cdot \lambda \cdot k^2), \tag{5}$$

where Δf is defocus, Cs the spherical aberration coefficient of the objective lens and λ the electron wavelength. By neglecting quadric components, the Fourier transform of the image intensity can be calculated as,

$$\Psi(\boldsymbol{k}) \otimes \tilde{\Psi}(\boldsymbol{k}) \cong \delta(\boldsymbol{k}) + 2\{A(\boldsymbol{k}) \sin\gamma(k) - B(\boldsymbol{k}) \times \cos\gamma(k)\}, \tag{6}$$

where $\tilde{\Psi}(\boldsymbol{k})$ represents the complex conjugate of $\Psi(\boldsymbol{k})$ and $B(\boldsymbol{k}) = B_0(\boldsymbol{k}) + B_{ef}(\boldsymbol{k})$. $\otimes$ denotes convolution. The term inside the parenthesis can be transformed to

$$\sqrt{A(\boldsymbol{k})^2 + B(\boldsymbol{k})^2}\,\sin\{2\pi(\tfrac{1}{4}Cs \cdot \lambda^3 \cdot k^4 - \tfrac{1}{2}\Delta f \cdot \lambda \cdot k^2) - \phi_a(\boldsymbol{k})\}, \tag{7}$$

where,

$$\phi_a(\boldsymbol{k}) = \arcsin\left\{\frac{B(\boldsymbol{k})}{\sqrt{A(\boldsymbol{k})^2 + B(\boldsymbol{k})^2}}\right\} = \arcsin Q(\boldsymbol{k}). \tag{8}$$

The sine term in Eq. (7) is called the contrast transfer function, CTF. Throughout this report, we define $Q(\boldsymbol{k})$, the ratio (%) of the attenuation term to the total contrast, as the amplitude contrast. In unfiltered imaging, $Q_0(\boldsymbol{k})$, which is defined as $Q(\boldsymbol{k})$ with $B_{ef}(\boldsymbol{k}) = 0$ has been empirically treated as a constant, Q_0 over all spatial frequencies. This assumption has not caused any serious problem up to ~4 Å resolution (Yonekura et al., 2003a). However, we do not know if the same holds for zero-loss imaging, where $B_{ef}(\boldsymbol{k})$ is not zero.

From Eq. (7), there is a zero-crossover point at a low spatial frequency only in images recorded at overfocus ($\Delta f < 0$; Fig. 2a). The amplitude contrast value, $Q(\boldsymbol{k})$ at a low spatial frequency can be estimated from the position of this zero point and the amount of defocus (Typke and Radermacher, 1982; Toyoshima et al., 1993).

2.2. Sample preparation and electron microscopy

Flagellin was isolated from *Salmonella typhimurium* strain SJW1655 and the R-type straight flagellar filament

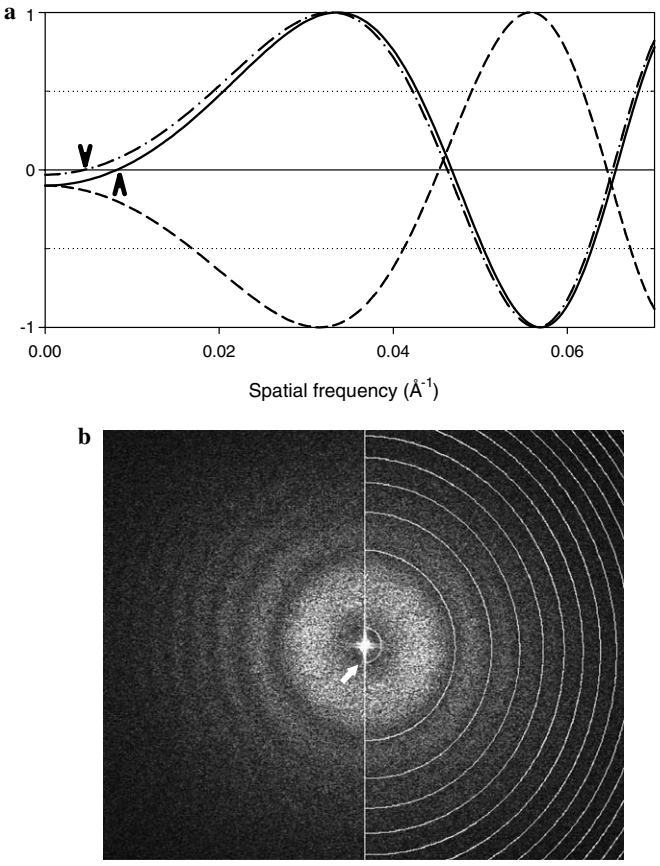

Fig. 2. Theoretical CTF curves (a) and Fourier transform of the carbon film (b). (a) CTF curves with spherical aberration, Cs = 2.2 mm and an accelerating voltage of 300 kV. Envelope function was omitted. Dash line: a defocus amount of 24 000 Å with the amplitude contrast of 10% treated as a constant all over spatial frequencies. (Solid line) The same as the dash line but a defocus amount of −24 000 Å (negative means overfocus). (Dash-dot line) The same as the solid line but with the amplitude contrast of 3%. Arrowheads indicate the CTF zero points at low spatial frequencies characteristic of the CTF with overfocus. (b) The CTF parameters were determined as follows: mean defocus = −23 900 Å, astigmatic focus difference = 1400 Å and azimuth of the minimum defocus from the horizontal = −75.3° (Tani et al., 1996). Circles indicating the CTF zero points are overlaid. Arrow indicates the 1st CTF zero point as the arrowheads in (a). The 2nd CTF zero point corresponds to ~21 Å.

was reconstituted as previously described (Mimori et al., 1995). The filaments were suspended in 0.15 M NaCl, 2 mM $MgCl_2$ and 20 mM Tris–HCl, pH 7.8. A few microliters of the sample was applied to a holy carbon film on a copper grid (Quantifoil R1.2/1.3, Quantifoil Micro Tools GmbH), and rapidly frozen by plunging into liquid ethane with a Vitrobot (FEI). Frozen-hydrated filaments were examined at ~−190 °C with an FEI G2 Polara F30 electron microscope, which is equipped with a field emission gun operated at an accelerating voltage of 300 kV and a post-column energy filter, GIF (Gatan). An energy slit was adjusted to select only electrons with energy loss less than 10 eV. With this setting of the slit, we can exclude most of electrons with plasmon loss in ice (Langmore and Smith, 1992) and carbon. An objective aperture with

the nominal diameter of 70 μm, which cuts electrons scattered beyond ~12 mrad corresponding to a spatial frequency of ~1/1.6 $Å^{-1}$, was always in place. Images were recorded on a 4k × 4k Gatan UltraCam slow-scan CCD (SSCCD) camera at a final magnification of ~110 000× at defocus settings of −15 000 to −40 000 Å (negative values represent overfocus). The SSCCD camera employs a beryllium mirror and a 14 element optical lens coupling for improving its point-spread function. The pixel size of the SSCCD camera is 15 μm and a final sampling is ~1.35 Å/pixel. A total electron dose of 16–25 $e^{-}/Å^{2}$ was used to record each single frame, which always included a carbon area. At least two images of the same view were taken with and without energy filtering at the same defocus setting, in either of the two different orders.

The thickness of ice (t) was estimated from the ratio of filtered (I_{+ef}) to unfiltered intensity (I_{-ef}) as,

$$t/\Lambda = \ln(I_{-ef}/I_{+ef}), \quad (9)$$

where Λ is the mean free path of inelastically scattered electrons (Egerton and Leapman, 1995). To estimate Λ, a hole was burnt in thick vitreous ice with the specimen stage tilted to +30° and then it was imaged with and without energy filtering but with the stage tilted to −30° (Angert et al., 1996).

For helical reconstruction, images were taken with energy filtering at an underfocus value of 12 000–20 000 Å.

2.3. Image analysis

Images of flagellar filaments were initially analyzed with a GUI program set as previously described (Yonekura et al., 2003b) with slight modifications. Briefly, the program XDISPBOX was newly developed for initial screening of filaments and the carbon film in a CCD image (Fig. 3), and the program GBOX for extracting selected areas with quadratic interpolation to a new sampling raster. Well-diffracting filaments were further analyzed to determine the repeat distance and the in-plane rotation angle of the helix axis (Toyoshima, 2000; Yonekura et al., 2003b). The center position of the helix axis was roughly adjusted by calculating the auto-correlation of one-dimensional projections along the helix axis (program PRJCENH), and applied to the control file (program HBOXCENH). This procedure reduces the error in subsequent steps that precisely determine the center position and the out-of-plane tilt (Toyoshima, 2000; Yonekura et al., 2003b). The actual magnification of each image was determined from an axial layer-line at 25.7 Å with the Bessel order of 1 (Maki-Yonekura et al., 2003). The program

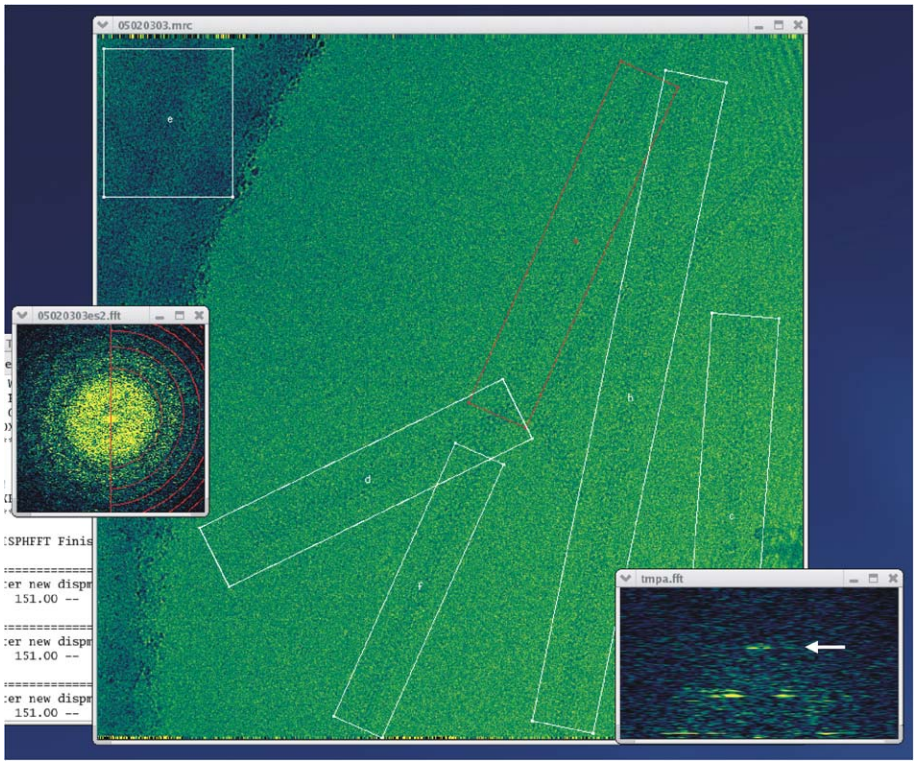

Fig. 3. A typical image recorded with a 4k × 4k SSCCD camera displayed with XDISPBOX in the X-Window system. Boxes enclose areas used for initial screening of the filaments and the carbon film. The Fourier transform of the filament enclosed with a red box shows clear layer lines (lower right). Arrow indicates a layer-line at an axial spacing of 25.7 Å. Box parameters were further refined as previously described (Yonekura et al., 2003b) to be included in the helical reconstruction shown in Fig. 10. The Fourier transform of the carbon area enclosed with a box at the upper left corner is also displayed.

Please cite this article as: Koji Yonekura et al., Electron energy filtering significantly improves amplitude ..., Journal of Structural Biology (2006), doi:10.1016/j.jsb.2006.07.016

set works under LINUX and MacOSX workstations, and is available on request.

The CTF parameters were first determined from the Fourier transform of the carbon film as described (Tani et al., 1996), assuming an amplitude contrast of a few percent for unfiltered images and ~10% for filtered ones. Several programs such as PLTCTFX, SCTRAVGFT, and CTFFIT were modified to support the overfocus range.

Then, rotational averaging of the amplitude spectrum was carried out for overfocused images of filaments and the carbon film by taking the astigmatism into account. Because the equatorial layer line in the Fourier transform of the filament image has a large structure factor, the equator and the data within a height of a few pixels from it were excluded from averaging. There were no other layer lines within this low spatial frequency range. The amplitude contrast value was estimated from the defocus amount and the position of the minimum point in the radial profile that corresponds to the 1st zero point of the CTF with overfocus. At least 4 data sets were extracted from a single view for filtered and unfiltered images of a filament and those of the carbon film. A total of 25 out of 32 pairs were used to calculate the average of the amplitude contrast for each of the 4 data sets. The remaining 7 pairs that showed no clear minimum were discarded. Then, using the average of the obtained amplitude contrast, the CTF parameters were determined again, and the amplitude contrast was estimated again as described above.

Helical reconstruction was carried out from the images taken at underfocus, as previously described (Yonekura et al., 2005). Spline fitting, box refinement, three-dimensional unbending, solvent flattening and scaling correction to the atomic model were not applied here.

3. Results

3.1. Effects of energy filtering on images

As reported previously (e.g. Schröder et al., 1990; Langmore and Smith, 1992; Zhu et al., 1997), images taken with energy filtering show much higher contrast than those without (Fig. 1). Upper and middle curves in Fig. 4 are projections along the filament axis of the same filament imaged with energy filtering in the 1st exposure (middle) and without it in the 2nd exposure (upper). There is a deep trough at the center corresponding to the central channel of the bacterial flagellar filament and two high peaks at radii of ~25 and ~45 Å, corresponding to the inner tube (domain D0) and the outer tube (D1), respectively, which form the filament core (Yonekura et al., 2001, 2003a). Densities corresponding to the outer domains (domain D2 and D3), which extend to a radius of ~120 Å, are minor contributors to the projections. The lower curve is a projection of another filament imaged with energy filtering in the 1st exposure and at underfocus, where the contrast was reversed. The image contrast was much improved and statistical noise was substantially reduced in the projections of the filtered

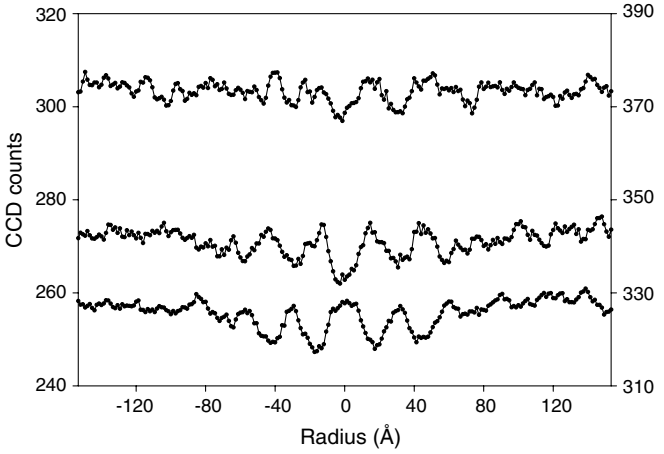

Fig. 4. Projections along the filament axis. The same filament was taken with energy filtering (middle) in the 1st exposure and without it in the 2nd exposure (upper) at the same defocus amount of ~−21 000 Å (overfocus). Box parameters including the in-plane rotation of the helix axis and the repeat distance were adjusted (Yonekura et al., 2003b). Structure features are; a valley at a radius of 0 Å corresponding to the central channel, two peaks at ~25 and ~45 Å to the inner (domain D0) and outer tubes (D1), respectively, a valley between them to the spoke region, and a outer part at radii of 70–120 Å to the outer domains (D2 and D3) (Yonekura et al., 2001, 2003a). The lower curve is a projection of another filament imaged with energy filtering in the 1st exposure at defocus of ~19 000 Å (underfocus). The contrast is reversed from those taken at overfocus (upper and middle). S/N (c/σ) defined as Eq. (10) is 0.065 for the upper, 0.170 for the middle and 0.183 for the lower. The labels on the left side represent CCD counts for the filtered image and those on the right side for the unfiltered one.

images (Fig. 4), as previously reported in cryo-images of tobacco mosaic virus (Langmore and Smith, 1992). However, due to radiation damage (data not shown) the differences between an unfiltered image taken in the 1st exposure and a filtered in the 2nd exposure are less obvious. To quantitatively evaluate the improvement, S/N or contrast/standard deviation (c/σ) was defined as,

$$c/\sigma = \frac{|\overline{I}_{\text{protein}} - \overline{I}_{\text{ice}}|}{\sigma_{\text{ice}}}, \tag{10}$$

where $\overline{I}_{\text{protein}}$ and $\overline{I}_{\text{ice}}$ represent the average intensity of protein embedded in ice and that of ice alone, respectively, and σ_{ice} the standard deviation within the ice region. The outer domains of the filament show low intensities compared to the inner core domains (Fig. 4). Also, boundaries between protein and ice usually show artificial edges with high contrast as a consequence of the CTF. Hence, those parts, which cover radii of 70–125 Å (Fig. 4) were excluded from calculation of c/σ. Radii of 0–70 Å were taken for $\overline{I}_{\text{protein}}$ and those of 125–160 Å $\overline{I}_{\text{ice}}$ and σ_{ice}. Table 1 summarizes c/σ for 22 pairs of different filtered and unfiltered images taken in either of the two collection orders. For these calculations, the original two-dimensional images and not one-dimensional projections were used. Here, 17 of the image pairs were recorded at overfocus and 5 pairs at underfocus. While the image contrast is substantially altered by defocus, the S/N was essentially the same for all the imag-

Table 1
Signal-to-noise ratio (S/N) of filtered and unfiltered images of frozen-hydrated protein

Energy filtering	Order to be recorded	Number of images	Average intensity (CCD counts)	Contrast[a] (CCD counts)	σ_{ice}[b]	S/N[c] (c/σ)[c]
+	Total	22	325.1	4.52	25.6	0.177
	1st exposure[d]	11	300.2	4.40	24.7	0.179
	2nd exposure[e]	11	350.0	4.64	26.4	0.176
−	Total	22	449.2	2.68	29.6	0.091
	1st exposure[e]	11	474.4	2.92	30.3	0.096
	2nd exposure[d]	11	424.1	2.44	28.8	0.085

[a] Defined as the numerator of Eq. (10).
[b] Defined as the denominator of Eq. (10).
[c] Defined as Eq. (10).
[d] Pairs from the same views.
[e] Pairs from the same views.

es; including both overfocused and underfocused images. The standard deviation of the S/N was especially low among all the data sets with energy filtering (0.017). The table also indicates that energy filtering improved the numerator, $|\overline{I}_{protein} - \overline{I}_{ice}|$ more than the denominator, σ_{ice} of Eq. (10). As is clear from the data, energy filtering resulted in an approximate 2-fold improvement in the S/N. This is essentially equivalent to imaging the sample at four times the electron dose.

3.2. Effects of energy filtering on layer lines

We also examined the effects of the energy filtering in Fourier space. To do so, background intensity (see Fig. 4) was first subtracted from each filament image (Toyoshima et al., 1993; Toyoshima, 2000) and then box parameters were determined (Toyoshima, 2000; Yonekura et al., 2003b). Fig. 5a shows the mean radial amplitude spectra of a typical pair of filtered and unfiltered images. Even after the subtraction of the mean intensity, the background level of the unfiltered one was still higher over all higher spatial frequency ranges. Fourier transformation of an image of the flagellar filament gave rise to 5 major layer lines up to an axial spacing of ~25 Å as shown in Fig. 5b. The numbers in each parenthesis represent the $(h,k;n)$ index of the corresponding layer-line (Toyoshima, 2000). To quantitatively evaluate the layer lines, intensity data statistics (I/σ) was defined as,

$$I/\sigma = \frac{I_{pk} - I_{bg}}{\sigma_{bg}}, \tag{11}$$

where I_{pk} represents average intensity of the 1st major peak of each layer line and I_{bg} and σ_{bg}, the average intensity and the standard deviation of neighboring pixels above and below the corresponding layer line, respectively. Here, the intensities, I_{pk} and I_{bg} represent the square of amplitude. For comparison, we selected 14 pairs of unfiltered and filtered images, which gave rise to shaper layer lines, out of those in Table 1. I/σ would be affected by the quality of the helical lattices and also the CTF, and the effect of radiation damage in the 2nd exposure must have been more severe as the spatial frequency is increased. Hence, the comparison is relatively qualitative. Table 2 indicates that I/σ was substantially improved by energy filtering in all layer lines examined (Fig. 5b). The improvement was significant even in relatively weaker ones, (−1, 1; −16) and

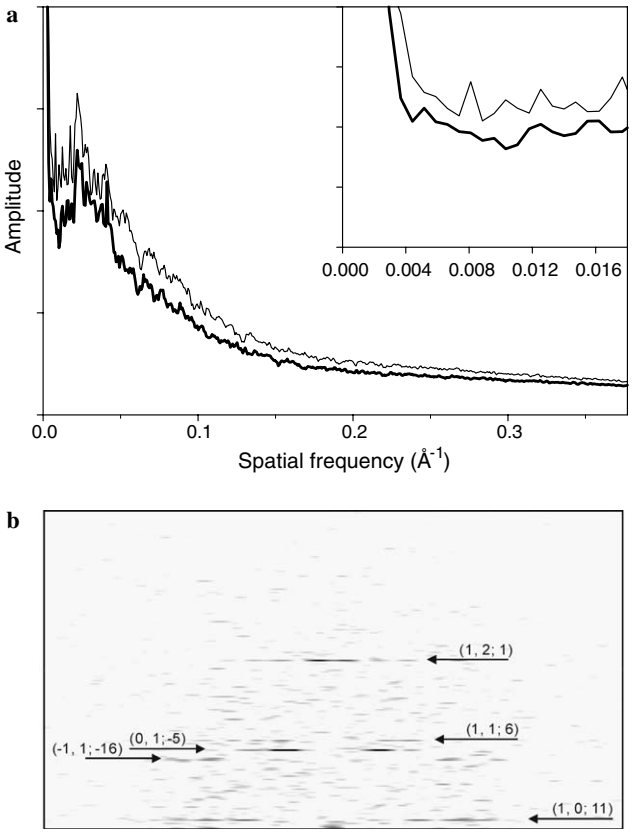

Fig. 5. Mean radial amplitude distribution of the Fourier transforms of a flagellar filament imaged with and without energy filtering (a) and Fourier transform of a filament image with energy filtering (b). (a) Calculated from a typical pair of a filtered (thick line) and unfiltered images (thin line) after subtraction of the mean density. The images were recorded at defocus of ~17 000 Å (underfocus). Inset at the upper right corner represents a magnified view of low-resolution part. (b) Fourier transform after box parameters were refined. Arrows and numbers in parentheses indicate major layer lines and their (h, k; n) indexes (Toyoshima, 2000). The axial spacing of each layer line is 446.1 Å for (1, 0; 11), 62.2 Å for (−1, 1; −16), 54.6 Å for (0, 1; −5), 48.7 Å for (1, 1; 6) and 25.7 Å for (1, 2; 1).

Table 2
Intensity data statistics (I/σ) of the 1st major peak[a] in layer lines from pairs of filtered and unfiltered images of frozen-hydrated flagellar filaments

Energy filtering	Order to be recorded	Number of peaks[b]	I/σ[c]				
			(1, 0; 11)[d]	(−1, 1; −16)[d]	(0, 1; −5)[d]	(1, 1; 6)[d]	(1, 2; 1)[d]
+	Total	28	5.90	6.67	47.35	10.95	15.55
	1st exposure[e]	14	6.17	7.94	40.32	10.39	19.08
	2nd exposure[f]	14	5.63	5.40	54.38	11.50	12.02
−	Total	28	5.65	5.02	38.0	8.57	11.90
	1st exposure[f]	14	5.69	4.33	52.44	11.49	14.70
	2nd exposure[e]	14	5.61	5.72	23.55	5.64	9.09

[a] A spatial frequency of the 1st major peak corresponds to a spacing of ~51 Å for (1, 0; 11), ~31 Å for (−1, 1; −16), ~47 Å for (0, 1; −5), ~41 Å for (1, 1; 6) or ~25 Å for (1, 2; 1).
[b] The number of images used was a half of that because each image gave two data sets from the near and far sides.
[c] Defined as Eq. (11).
[d] The (h, k; n) index (Toyoshima, 2000).
[e] Pairs from the same views.
[f] Pairs from the same views.

(1, 1; 6) and that at the highest resolution of those, (1, 2; 1). Even with more radiation damage, the filtered images taken in the 2nd exposure (the 3rd row in Table 2) have I/σ comparable to or better than the unfiltered ones in the 1st exposure (the 5th row), while the unfiltered ones in the 2nd exposure (the 6th row) have much lower I/σ (cf. the 2nd row). While this makes precise quantification difficult, it clearly indicates the benefits of energy filtering.

Next the layer-line data were averaged among filtered sets or unfiltered sets in Table 2 separately as described elsewhere. One of the data sets showed poor fitting of the phase residual to the others and was removed from the averaging. Using the layer-line data set computed from the atomic model of the flagellar filament (Yonekura et al., 2003a; Yonekura et al., 2005) as the reference data, inter-particle phase residuals were calculated as described previously (Yonekura and Toyoshima, 2000a; Yonekura and Toyoshima, 2000b). These data (Table 3) demonstrate that energy filtering improves the phase residuals by 7°–10° up to ~15 Å resolution, and by ~2° even in the 15–10 Å range. The maps calculated from both the data showed the same structural features (data not shown).

3.3. Amplitude contrast

A typical example of the Fourier transform of the carbon film recorded at overfocus is shown in Fig. 2b. An amplitude minimum at a very low spatial frequency (arrow in b) corresponds to the 1st zero point of the CTF with overfocus (arrowheads in Fig. 2a). Rotational averaging of the amplitude spectra clearly resolves these minimum points (arrows in Fig. 6), which depend on the degree of defocus and the amount of amplitude contrast. Two successive overfocused images (filtered and unfiltered) of the same filament and carbon film were used in Fig. 6. A pair of images taken at underfocus with and without energy filtering produced no such clear minimum points (inset in Fig. 5a). The amount of defocus could be accurately determined, independent of the first zero point, by using the higher frequency Thon rings in the Fourier transforms of the carbon film (Tani et al., 1996). The amount of amplitude contrast was estimated from a total of 25 images for each data set as shown in Fig. 6. Their minimum points were distributed over 1/350–1/100 $Å^{-1}$. Estimated values were plotted against defocus amounts in Fig. 7. Although they are relatively widely distributed, filtered images of the carbon film show the highest amount of amplitude contrast, followed by filtered ones of protein, unfiltered images of the carbon film, and unfiltered ones of protein, a ranking which is consistent with the pairs of filtered and unfiltered images as seen in Fig. 6. The average values are $9.5 \pm 2.0\%$, $6.9 \pm 1.9\%$, $5.8 \pm 1.8\%$ and $2.7 \pm 1.0\%$, respectively (Table 4).

Table 3
Inter-particle fitting phase residuals[a] (°) of averaged data to the reference data

Energy filtering	Number of averaged images	Resolution range ($Å^{-1}$)			
		0–1/25	1/20–1/15	1/15–1/10	Overall
+	13	25.4	51.3	69.9	44.1
−	13	32.2	61.0	71.7	50.4
Number of data points used for the calculation[b]		213 (73.5%)	311 (28.1%)	163 (13.9%)	687 (26.7%)

[a] Amplitude weighted inter-particle phase residual, fitted to the reference data built from the atomic model of the flagellar filament (Yonekura et al., 2003a, 2005). The calculation used all the points with amplitudes higher than 5.0% of the highest off-equatorial peak. The equator was omitted from the calculation. A value of 90° means that the phases are uncorrelated.
[b] Number in parentheses represents the percentage of data points used for the calculation to all possible points (Yonekura and Toyoshima, 2000a,b).

Please cite this article as: Koji Yonekura et al., Electron energy filtering significantly improves amplitude ..., Journal of Structural Biology (2006), doi:10.1016/j.jsb.2006.07.016

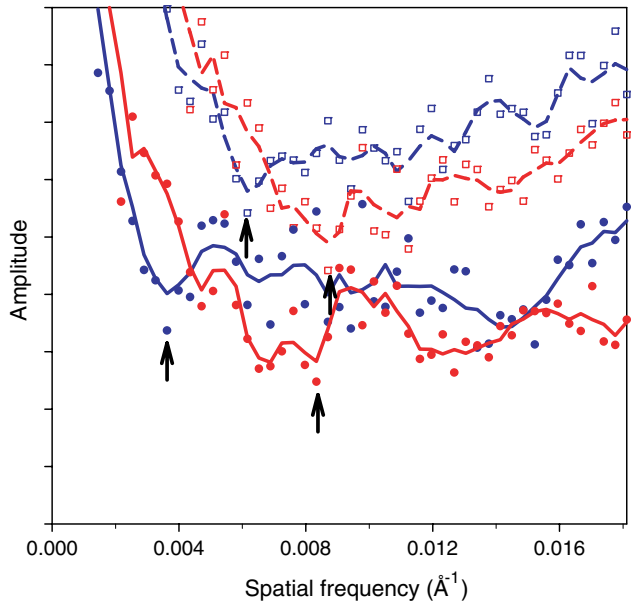

Fig. 6. Mean radial amplitude distribution of the Fourier transforms from a flagellar filament and the carbon film recorded at overfocus in the same view. Red and blue symbols represent filtered data in the 1st exposure and unfiltered ones in the 2nd exposure, respectively, and filled and open symbols from the filament and the carbon film. Curve lines represent running averages of data points. Both of the filtered and unfiltered were recorded at defocus of ~−19000 Å. Arrows indicate the 1st CTF zero points as in Fig. 2a and b. The amplitude contrast was estimated from the positions of these points and the defocus amounts, and was 8.1% for the filtered filament, 9.0% for the filtered carbon film, 1.6% for the unfiltered filament and 4.7% for the unfiltered carbon film.

3.4. The thickness of ice

Energy filtering allows measuring the thickness of ice as in Eq. (9). First, the mean free path, Λ for inelastically scattered electrons at 300 kV was measured to be ~4000 Å from a tilted view of a hole in thick vitreous ice imaged with and without energy filtering (Angert et al., 1996). Grimm et al. (1996) and Feja and Aebi (1999) measured $\Lambda = 2000$–2500 Å at 120 kV, which can be converted into 3500–4400 Å at 300 kV by multiplying it by the factor, $(\beta_{300}/\beta_{120})^2 = (0.7765/0.5867)^2$, where β_{120} and β_{300} are the ratios of the electron velocity at 120 and 300 kV to that of light, respectively. Our estimate seems to be in good agreement with their values (Grimm et al., 1996; Feja and Aebi, 1999).

With Λ of 4000 Å, the thickness of ice surrounding each filament was estimated from the filtered and unfiltered pairs used in Fig. 7. Then, the amplitude contrast of protein was plotted against the ice thickness in Fig. 8. The data suggest a weak dependence of amplitude contrast on the ice thickness in filtered images, and none in the unfiltered ones.

Table 4
Amplitude contrast with and without energy filtering at an accelerating voltage of 300 kV

Energy filtering	Number of images	Amplitude contrast (%)	
		Protein embedded in ice	Carbon film
+	25	6.9 ± 1.9	9.5 ± 2.0
−	25	2.7 ± 1.0	5.8 ± 1.8

3.5. Three-dimensional map of the flagellar filament

Using the amplitude contrast of 6.9% thus obtained as a constant over all spatial frequencies, helical reconstruction was carried out from 54 filtered images taken at underfocus as previously described (Yonekura et al., 2003b). The mean radial density distribution (MRDD) is highly sensitive to the amplitude contrast and hence provides a good criterion for assessment. The MRDD of the averaged data set in Fig. 9 has densities close to zero at the central channel,

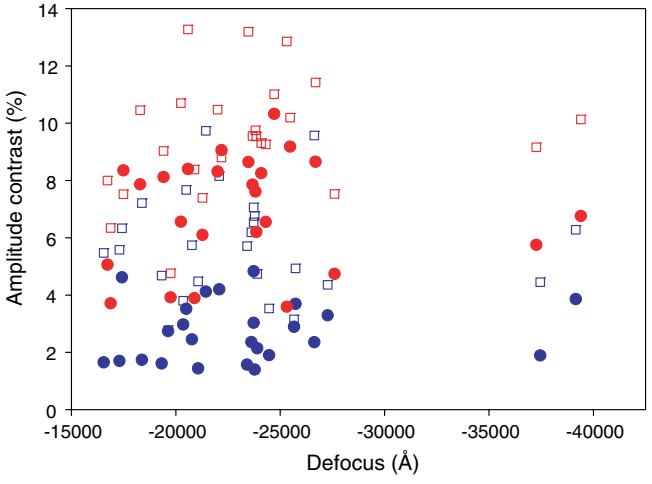

Fig. 7. Distribution of the amplitude contrast from flagellar filaments or the carbon film plotted against defocus. Red and blue symbols represent filtered and unfiltered data, respectively, recorded in either the 1st or 2nd exposure, and filled and open symbols indicate the filaments or the carbon film, respectively.

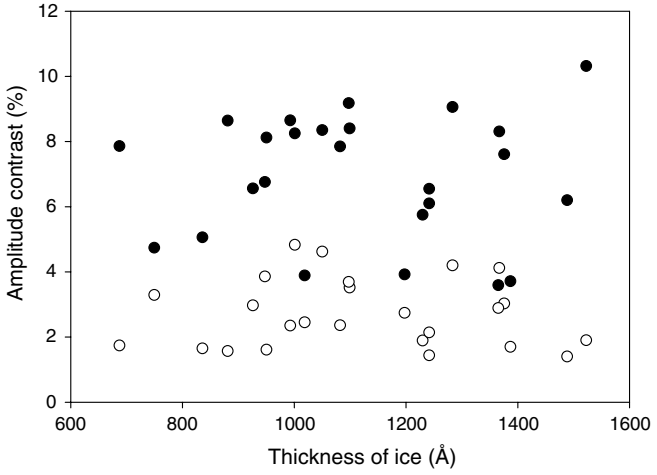

Fig. 8. Distribution of the amplitude contrast of frozen-hydrated flagellar filaments plotted against the thickness of ice. The data sets are the same as in Fig. 7. Filled and open circles represent filtered and unfiltered data, respectively.

Please cite this article as: Koji Yonekura et al., Electron energy filtering significantly improves amplitude ..., Journal of Structural Biology (2006), doi:10.1016/j.jsb.2006.07.016

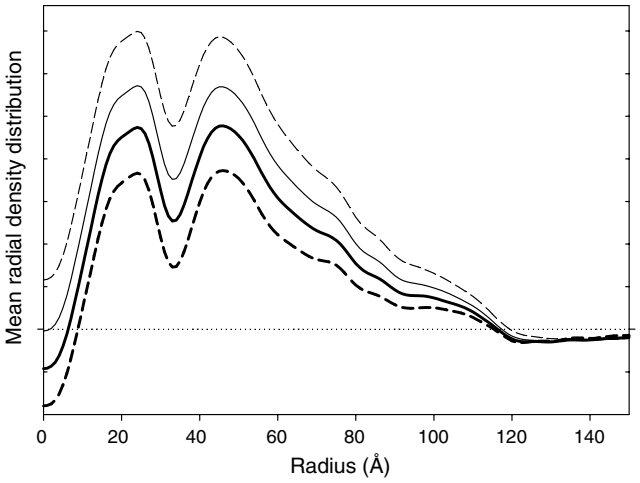

Fig. 9. Mean radial density distribution (MRDD) of the average of filtered flagellar filament images taken at underfocuses. An amplitude contrast of 4% (thin dash line), 5.3% (thin solid line), 6.9% (thick solid line) or 10% (thick dash line) was used as a constant for each curve. Scaling was adjusted among the data sets by using layer lines excluding the equator before the amplitudes were corrected for the CTF.

shows two clear peaks for the inner and outer tubes, and outer domains extending to ~120 Å. This is a good match to the known structure. Applying an amplitude contrast of 4% or 10% produced an MRDD with higher or lower density in the central channel, respectively (Fig. 9). An amplitude contrast of ~5.3% gave exact zero at the center (thin solid line in Fig. 9; Table 5). For the averaged data without energy filtering shown in Table 3, applying an amplitude contrast of ~3.5% produced an MRDD with zero at the center, but these values are still within error tolerances (Tables 4 and 5).

Fig. 10a shows the three-dimensional structure calculated at ~8 Å resolution, in to which a part of the atomic model (Yonekura et al., 2003a) is superimposed. The map clearly resolves the α-helical coiled-coil structures both in domains D0 and D1 of the filament core (Yonekura et al., 2003a), justifying the resolution stated for this map. An amplitude contrast of ~5.3% produced a similar map to Fig. 10a (data no shown). When applying the amplitude contrast of 4 or 10%, overall densities in the three-dimensional map were incorrect (Fig. 10b and c) compared with that in Fig. 10a and the previous map (Yonekura et al., 2003a).

4. Discussion

Obtaining accurate values for the amount of amplitude contrast is an important factor in the accurate reconstruction of three-dimensional structures of biological macromolecules. It has been reported that the amplitude contrast is increased in images taken with energy filtering at accelerating voltages of 80 and 120 kV (Langmore and Smith, 1992; Zhu et al., 1997; Angert et al., 2000). Here, we directly measured the amplitude contrast from frozen-hydrated protein imaged with and without energy filtering at 300 kV, and applied it to helical reconstruction from filtered images of the bacterial flagellar filament.

Table 5
Reported values of the amplitude contrast of frozen-hydrated biological molecules so far

Accelerating voltage (kV)	Energy filtering	Amplitude contrast (%)	Sample	Method	Reference
120	–	7[a]	Tubular crystal of membrane protein	Ratio of diffraction spots from a focal pair	Toyoshima and Unwin (1988)
80	+	14.0	Tobacco mosaic virus (protein + RNA)	Shape of the equatorial layer line of an averaged data	Smith and Langmore (1992)
120	–	5.5–6.0	Tubular crystal of membrane protein	1st zero point of the equatorial layer line from an overfocused image	Toyoshima et al. (1993)
200	–	4.6 ± 0.27	Same as above	Same as above	Toyoshima et al. (1993)
120	–	9	Ribosome (protein + RNA)	Computational model fitting	Zhu et al. (1997)
120	+	14	Same as above	Same as above	Zhu et al. (1997)
400	–	8.2 ± 5.2	Virus capsid protein	Solution X-ray scattering	Thuman-Commike et al. (1999)
120	+	15.5 ± 3.67	Actin-myosin filament (protein)	Computational model fitting	Angert et al. (2000)
200	–	6 ± 2	RNA + protein particle	Computational model fitting	Sander et al. (2003)
120	–	7.6 ± 0.4	GroEL (protein)	Computational model fitting	Mallick et al. (2005)
300	–	2.7 ± 1.0	Flagellar filament (protein)	1st minimum of the mean radial amplitude spectrum of an overfocused image	This work
300	+	6.9 ± 1.9	Same as above	Same as above	This work
300	–	3.5	Same as above	Value at the innermost radius on the equatorial layer line of an averaged data	This work
300	+	5.3	Same as above	Same as above	This work

[a] The sample was on the carbon film.

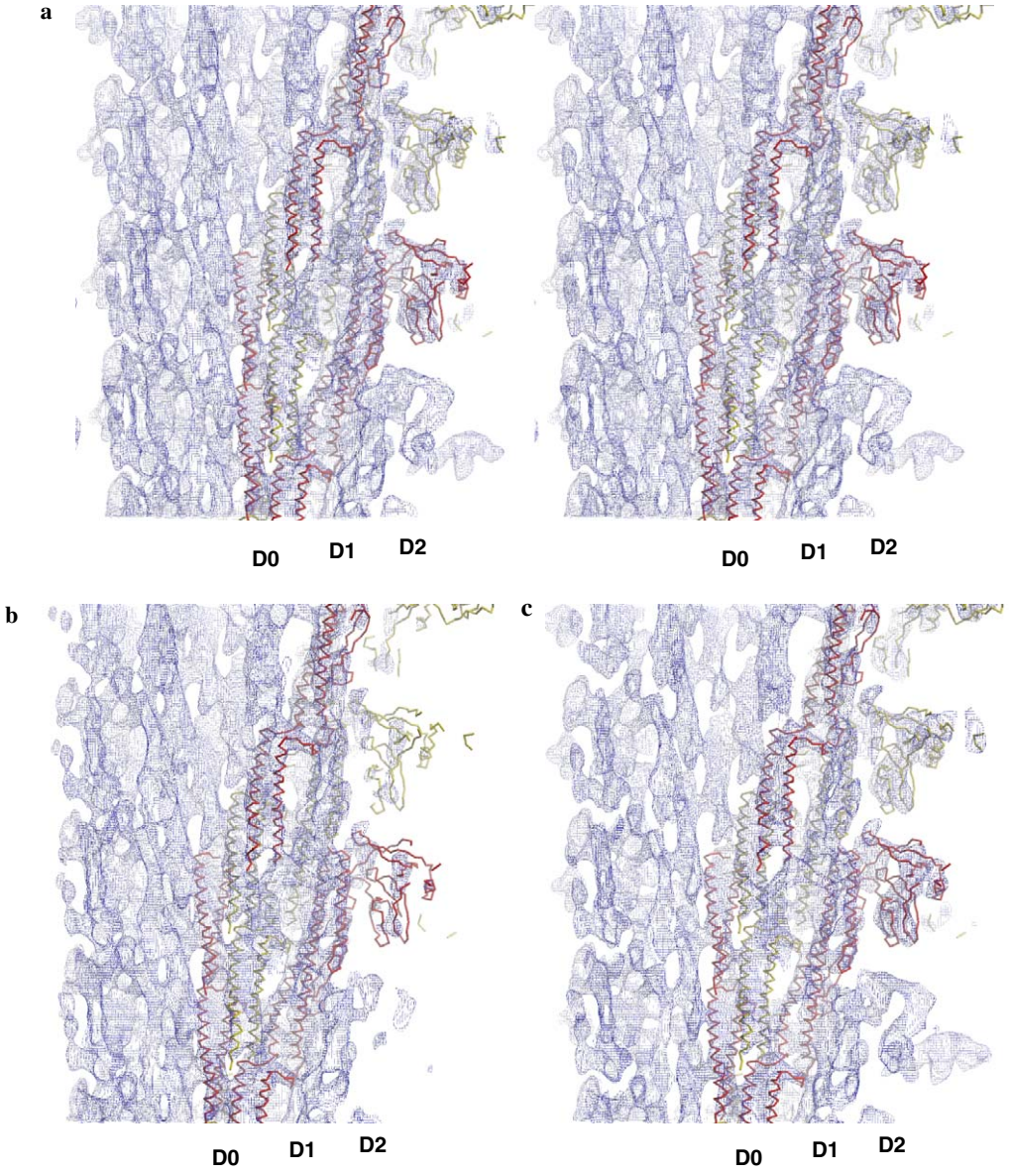

Fig. 10. Three-dimensional maps of the bacterial flagellar filament calculated at 8 Å resolution. Viewed from inside the filament. A total 54 images corresponding to ~17700 molecular images were averaged. (a) An amplitude contrast of 6.9% was used as a constant. Stereo view. (b) An amplitude contrast of 4% was used as a constant. (c) Same as (b) but an amplitude contrast of 10% was used. Contour levels of all the maps are $\sim 2\sigma$. The atomic models of flagellin (Yonekura et al., 2003a) were superimposed on part of the density map. Note that α-helical coiled coil structures in domains D0 and D1 are nicely fitted into the map. Compared to the previous map (Yonekura et al., 2003a), densities of the outer domains become lower in (b) but higher in (c), while densities of the inner domains become lower in (c), which features correspond to the MRDDs in Fig. 9. The map in (a) shows a correct overall density distribution.

4.1. The effects of energy filtering

Energy filtering has dramatically improved intensity data statistics in electron diffraction from two-dimensional and thin three-dimensional protein crystals (Yonekura et al., 2002). Although there are many reports to claim that energy filtering improves the image contrast and S/N (Schröder et al., 1990; Langmore and Smith, 1992; Zhu et al., 1997; Grimm et al., 1998), quantitative evaluation has been missing for frozen-hydrated samples and exact degree of improvement has not been clearly determined in image mode. We have introduced a new measure of the S/N or contrast/standard deviation (c/σ) that should best correspond to feature detectability and further showed that energy filtration improves it by approximately a factor of two in images of frozen-hydrated protein samples. The improvement can be considered to originate from two major effects of energy filtering: First, inelastically scattered electrons, which contribute incoherently to the image at moderate and high resolutions, are removed, which leads to reduction of σ_{ice} (Table 1). Second, removing these inelastic electrons via the energy slit acts as a virtual source of amplitude contrast enhancement, as reflected in an increase of $|\overline{I}_{\mathrm{protein}} - \overline{I}_{\mathrm{ice}}|$ (Table 1). The latter term appears

Please cite this article as: Koji Yonekura et al., Electron energy filtering significantly improves amplitude ..., Journal of Structural Biology (2006), doi:10.1016/j.jsb.2006.07.016

to be dominant (Table 1). These effects are especially beneficial in single-particle image analysis, where they act to significantly improve the ability of picking and aligning individual molecular images. Importantly, the twofold contrast enhancement is equivalent to being able to work at a fourfold higher dose level at least for feature detectability.

To understand the frequency content of the increased contrast, we examined the effect of energy filtering in Fourier space which revealed that the layer line intensity data statistics (I/σ) was much improved up to ~25 Å resolution by energy filtering (Table 2). The beneficial effects of energy filtering might actually extend to higher resolution, as the background level is still decreasing at higher spatial frequencies (Fig. 5a). This is confirmed since the inter-particle phase residuals of the averaged data sets also revealed remarkable improvement up to ~15 Å by energy filtering (Table 3). Therefore, energy filtering must be very effective not only for single-particle image analysis but also for analysis of any crystalline sample, such as two-dimensional crystals and helical assemblies. However, the improvement from energy filtering was not as large as in electron diffraction (Yonekura et al., 2002), presumably because the average of background counts arising from unscattered and inelastically scattered electrons was first subtracted here. The improvement of I/σ and the phase residual came mainly from reduction of noise since the effect of the increased amplitude contrast only contributes in the very low spatial frequency range.

4.2. Measurement of the amplitude contrast

To measure the amplitude contrast accurately, we have introduced a simple and reliable method and applied it to images of the bacterial flagellar filament embedded in vitreous ice. Toyoshima et al. (1993) used a zero-crossover point at low spatial frequency in the equatorial layer line from tubular crystals of membrane protein imaged at overfocus. However this approach did not work properly for the bacterial flagellar filament as it is critically dependent on precise background subtraction as discussed by Toyoshima et al. (1993). Using this approach was probably hampered by the relatively poor S/N in a single image of the flagellar filament analyzed, which usually contains several hundred molecules with a diameter of 240 Å, while that of a tubular crystal of membrane protein contains more than 1000 molecules with a diameter of 600–900 Å. By contrast, our method is based on determining the minimum point in a rotational average excluding the equator (Fig. 6), which is less affected by background subtraction effects. Using this approach, the amplitude contrast of the flagellar filament embedded in vitreous ice was measured and shown to be substantially increased by energy filtering (Tables 4 and 5; Fig. 7). The values appear to be more dispersed than in the previous report (Toyoshima et al., 1993). In principle, if background subtraction is sufficiently accurate, the previous method might allow more accurate estimates as it uses the equatorial layer line, which has a relatively high S/N. Our attempts with the flagellar filament look to be rather variable (Fig. 7), but this might also be due to a weak dependence on the ice thickness especially for the filtered images as in Fig. 8.

We applied the same method of measurement to the carbon film and also showed a significant increase in the amplitude contrast with energy filtering (Table 4; Fig. 7). The measurement could be reasonable since the carbon film scattered more electrons both elastically and inelastically than protein, resulting in an increase in the amplitude contrast. Our method would be applicable for other types of samples, e.g. mono-dispersed biological macromolecules such as ribosomes, chaperonins, etc.

Importantly, the increased amplitude contrast made possible by energy filtering should allow imaging at lower amounts of defocus than would otherwise be possible in unfiltered imaging because of poor contrast. Not only does imaging closer to focus move the zero-crossovers out toward higher spatial frequencies and decrease the rate of oscillation, but it would also improve the envelope function of the CTF even when using a field emission gun. The result would be quite significant improvement in both resolution and alignability.

4.3. Other reports

There have been a number of reports on estimation of amplitude contrast from proteins and also protein–nucleic acid complexes embedded in ice, as shown in Table 5, about half of which used computational model fitting. While amplitude contrast is dominant at very low spatial frequencies, there is a high background arising from the direct electron beam that makes accurate measurements difficult at such low frequencies. The approach outlined here is easily carried out, and is less sensitive to high background and also radiation damage.

Previously, all reports except for one on amplitude contrast have been based on measurements at 200 kV or lower. However, increasingly, 300 kV is becoming a standard voltage for high-resolution structure analysis of biological molecules. The scattering cross-section of electrons for proteins decreases at the higher voltages, resulting in a decrease in the amplitude contrast. Nucleic acids scatter more electrons than protein, resulting in an increase in the amplitude contrast of protein–nucleic acid complexes. Therefore the determined amplitude contrast (Tables 4 and 5) seems to be reasonable for frozen-hydrated protein with no nucleic acids imaged with and without energy filtering at 300 kV. The MRDD (Fig. 9) and the three-dimensional map (Fig. 10) also justified our conclusions about energy filtering.

4.4. Dependence on spatial frequency

Erickson and Klug (1971) examined the spatial frequency dependence of the amplitude contrast in images of negatively stained protein and showed little dependence up to ~25 Å resolution. Toyoshima and Unwin (1988) and Toyoshima

et al. (1993) used frozen-hydrated protein with no staining and showed that it would be constant over 1/350–1/35 Å^{-1}. As a consequence, amplitude contrast has been treated as a constant over the entire spatial frequency range in unfiltered imaging. This assumption seems to hold to at least ~4 Å resolution (Yonekura et al., 2003a). Angert et al. (2000) defined the filtered amplitude contrast, B_{ef} in Eq. (4) as a Gaussian function, which attenuates to a half at ~20 Å resolution. We did not examine the spatial frequency dependence because a poor S/N and severe radiation damage make accurate measurements difficult (Toyoshima and Unwin, 1988). Using the determined value of the amplitude contrast, we carried out helical reconstruction of flagella filaments. The three-dimensional density map calculated at 8 Å resolution resolved α-helical coiled coil structures as in the previous map (Yonekura et al., 2003a), indicating that assuming a constant amplitude contrast is justifiable probably because the phase shift introduced by the amplitude contrast has only a limited effect at intermediate to higher spatial frequencies. Furthermore, reconstructions calculated with smaller or larger values of amplitude contrast (Fig. 10b and c) were inferior to that using the measured value.

5. Conclusion

Energy filtering improves the S/N by about a factor of two in images of frozen-hydrated protein and substantially enhances the measured I/σ for layer lines up to at least ~25 Å resolution in the Fourier transforms of filament images. Inter-particle fitting phase residuals of the averaged data set indicate that the improvement extends to higher resolutions (at least ~15 Å). The amplitude contrast of frozen-hydrated protein was estimated as $6.9 \pm 1.9\%$ and $2.7 \pm 1.0\%$ with and without energy filtering, respectively, at an accelerating voltage of 300 kV. Increase of the amplitude contrast allows a lower defocus setting, which will lead to better imaging by shifting the position of the CTF zeros toward higher spatial frequencies, decreasing the rate of oscillation, and improving the envelope function. Using the value determined for the amplitude contrast of 6.9% as a constant over all frequencies, the three-dimensional map of the flagellar filament was calculated to a resolution of 8 Å. Treating the amplitude contrast in this way caused no serious errors in the reconstruction. The quality of the map and its mean radial density distribution validated the obtained value of the amplitude contrast and demonstrated the utility of SSCCD cameras to obtain high-resolution structural information.

Acknowledgments

We thank Keiichi Namba and John W. Sedat for support. We also thank Chikashi Toyoshima and Kazutoshi Tani for some of their programs. This work was supported by funds from the W.M. Keck Advanced Microscopy Laboratory at UCSF.

References

Angert, I., Burmester, C., Dinges, C., Rose, H., Schröder, R.R., 1996. Elastic and inelastic scattering cross-sections of amorphous layers of carbon and vitrified ice. Ultramicroscopy 63, 181–192.

Angert, I., Majorovits, E., Schröder, R.R., 2000. Zero-loss image formation and modified contrast transfer theory in EFTEM. Ultramicroscopy 81, 203–222.

Egerton, R.F., Leapman, R.D., 1995. Electron optics in imaging energy filters. In: Reimer, L. (Ed.), Energy-filtering Transmission Electron Microscopy, Springer, Berlin, pp. 269–290.

Erickson, H.P., Klug, A., 1971. Measurement and compensation of defocussing and aberrations by Fourier processing of electron micrographs. Phil. Trans. R. Soc. Lond. B261, 105–118.

Feja, B., Aebi, U., 1999. Determination of the inelastic mean free path of electrons in vitrified ice layers for on-line thickness measurements by zero-loss imaging. J. Microsc. 193, 15–19.

Grimm, R., Typke, D., Barmann, M., Baumeister, W., 1996. Determination of the inelastic mean free path in ice by examination of tilted vesicles and automated most probable loss imaging. Ultramicroscopy 63, 169–179.

Grimm, R., Typke, D., Baumeister, W., 1998. Improving image quality by zero-loss energy filtering: quantitative assessment by means of image cross-correlation. J. Microsc. 190, 339–349.

Langmore, J.P., Smith, M.F., 1992. Quantitative energy-filtered electron microscopy of biological molecules in ice. Ultramicroscopy 46, 349–373.

Maki-Yonekura, S., Yonekura, K., Namba, K., 2003. Domain movements of HAP2 in the cap-filament complex formation and growth process of the bacterial flagellum. Proc. Natl. Acad. Sci. USA 100, 15528–15533.

Mallick, S.P., Carragher, B., Potter, C.S., Kriegman, D.J., 2005. ACE: automated CTF estimation. Ultramicroscopy 104, 8–29.

Mimori, Y., Yamashita, I., Murata, K., Fujiyoshi, Y., Yonekura, K., Toyoshima, C., Namba, K., 1995. The structure of the R-type straight flagellar filament of *Salmonella* at 9 Å resolution by electron cryomicroscopy. J. Mol. Biol. 249, 69–87.

Sander, B., Golas, M.M., Stark, H., 2003. Automatic CTF correction for single particles based upon multivariate statistical analysis of individual power spectra. J. Struct. Biol. 142, 392–401.

Schröder, R.R., Hofmann, W., Ménétret, J.-F., 1990. Zero-loss energy filtering as improved imaging mode in cryoelectronmicroscopy of frozen-hydrated specimens. J. Struct. Biol. 105, 28–34.

Smith, M.F., Langmore, J.P., 1992. Quantitation of molecular densities by cryo-electron microscopy. Determination of the radial density distribution of tobacco mosaic virus. J. Mol. Biol. 226, 763–774.

Tani, K., Sasabe, H., Toyoshima, C., 1996. A set of programs for determining defocus and astigmatism in electron images. Ultramicroscopy 65, 31–44.

Thuman-Commike, P.A., Tsuruta, H., Greene, B., Prevelige Jr., P.E., King, J., Chiu, W., 1999. Solution X-ray scattering-based estimation of electron cryomicroscopy imaging parameters for reconstruction of virus particles. Biophys. J. 76, 2249–2261.

Toyoshima, C., Unwin, N., 1988. Contrast transfer for frozen-hydrated specimens: determination from pairs of defocused images. Ultramicroscopy 25, 279–291.

Toyoshima, C., Yonekura, K., Sasabe, H., 1993. Contrast transfer for frozen-hydrated specimens II. Amplitude contrast at very low frequencies. Ultramicroscopy 48, 165–176.

Toyoshima, C., 2000. Structure determination of tubular crystals of membrane proteins. I. Indexing of diffraction patterns. Ultramicroscopy 84, 1–14.

Typke, D., Radermacher, M., 1982. Determination of the phase of complex atomic scattering amplitudes from light-optical diffractograms of electron microscope images. Ultramicroscopy 9, 131–138.

Yonekura, K., Toyoshima, C., 2000a. Structure determination of tubular crystals of membrane proteins. II. Averaging of tubular crystals of different helical classes. Ultramicroscopy 84, 15–28.

Please cite this article as: Koji Yonekura et al., Electron energy filtering significantly improves amplitude ..., Journal of Structural Biology (2006), doi:10.1016/j.jsb.2006.07.016

Yonekura, K., Toyoshima, C., 2000b. Structure determination of tubular crystals of membrane proteins. III. Solvent flattening. Ultramicroscopy 84, 29–45.

Yonekura, K., Maki-Yonekura, S., Namba, K., 2001. Structure analysis of the flagellar cap-filament complex by electron cryomicroscopy and single-particle image analysis. J. Struct. Biol. 133, 246–253.

Yonekura, K., Maki-Yonekura, S., Namba, K., 2002. Quantitative comparison of zero-loss and conventional electron diffraction from 2D and thin 3D protein crystals. Biophys. J. 82, 2784–2797.

Yonekura, K., Maki-Yonekura, S., Namba, K., 2003a. Complete atomic model of the bacterial flagellar filament by electron cryomicroscopy. Nature 424, 643–650.

Yonekura, K., Toyoshima, C., Maki-Yonekura, S., Namba, K., 2003b. GUI programs for processing individual images in early stages of helical image reconstruction. For high-resolution structure analysis. J. Struct. Biol. 144, 184–194.

Yonekura, K., Maki-Yonekura, S., Namba, K., 2005. Building the atomic model for the bacterial flagellar filament by electron cryomicroscopy and image analysis. Structure 13, 407–412.

Zhu, J., Penczek, P.A., Schröder, R., Frank, J., 1997. Three-dimensional reconstruction with contrast transfer function correction from energy-filtered cryoelectron micrographs: procedure and application to the 70S *Escherichia coli* ribosome. J. Struct. Biol. 118, 197–219.

Please cite this article as: Koji Yonekura et al., Electron energy filtering significantly improves amplitude ..., Journal of Structural Biology (2006), doi:10.1016/j.jsb.2006.07.016